# Irradiation responses of an oxide-dispersion strengthened 15-15Ti austenitic stainless steel after He and D ion irradiations*

Ao-Xiang Gong,[1] Chun-Feng Shi,[2] Chao-Jun Luo,[1] Lu Sun,[1] Chi Xu,[3,†] and Zhen-Feng Tong[1,‡]

[1]*School of Nuclear Science and Engineering, North China Electric Power University, Beijing 102206, China*
[2]*CNNP Operation Maintenance Technology Co., Ltd, Hangzhou 330100, China*
[3]*Key Laboratory of Beam Technology of the Ministry of Education, School of Physics and Astrology, Beijing Normal University, Beijing 100875, China*

Microstructure of 15-15Ti steel and oxide-dispersion strengthened (ODS) 15-15Ti steel samples after D/He ion irradiations was characterized by transmission electron microscopy (TEM). High densities of dislocation loops were observed in both samples after He ion irradiation. Frank dislocation loops (FDL) in the edge-on geometry are clearly observed through the rel-rod dark-field technique. In addition, high densities of He bubbles were also observed in both samples. Radiation defects such as the "black-dot" defects were generated under D ion irradiation in both samples. The nanoindentation results indicate that irradiation hardening occurred in both samples, and it is shown that bubbles are weak strength obstacles, while dislocation loops are medium to strong strength obstacles. Radiation induced segregation (RIS) is observed at the grain boundaries of both samples after irradiation by the energy-dispersive spectrum analysis. Irradiation defects and irradiation effects observed for ODS samples are all lower than for 15-15Ti samples. The oxide particles stay stable in the irradiated ODS sample after different irradiation processes. The pinning of dislocation loops by oxide particles and the adsorption of He bubbles at the oxide particle/matrix interface can be observed, indicating the beneficial effects of the oxide particles in improving the irradiation resistance of the 15-15Ti steel.

Keywords: ODS steel, 15-15Ti austenitic stainless steel, Irradiation damage, He bubbles, TEM characterizations

## 1. Introduction

Fast breeder reactors (FBRs) as a next-generation (Gen IV) nuclear power technology may enable a closed-cycle nuclear fuel usage and will significantly improve the energy efficiency. Austenitic stainless steels (Au-SSs) are widely used as a reactor core structural material in FBRs due to the excellent creep performances and corrosion resistance, which are regarded as candidate materials for the Gen IV nuclear power reactors [1, 2]. Due to the face-centered cubic (FCC) crystal structure, Au-SSs are susceptible to irradiation swelling, limiting their use in nuclear energy systems [3]. The 15-15Ti Au-SS is selected as a cladding material for experimental and demonstration FBRs in China. Benefitting from the easy machinability of Au-SSs, methods have been employed to further improve the mechanical properties through optimizing the alloy compositions as well as through adding oxide-dispersion-strengthening particles in the 15-15Ti Au-SS matrix [4, 5]. The oxide dispersion strengthened (ODS) 15-15Ti Au-SS has provided significant improvements in terms of the mechanical strength etc. properties.

The ODS strategy has been widely employed in ferritic/martensitic (F/M) steels in order to improve their high-temperature mechanical properties [6, 7]. Compared to conventional F/M steels, Au-SSs have superior tensile and creep fracture strengths at elevated temperatures as well as the improved corrosion resistances [6]. However, the large irradiation swelling of Au-SSs at high doses may limit their use in commercial FBRs where the end-of-life irradiation dose of core components are considerably higher than those in experimental reactors. In cope of this problem, the ODS Au-SSs may provide superior irradiation resistance due to the large numbers of minute oxide particles dispersed in the austenite matrix. The ODS particles further improve the creep performances due to the obstacle effect of the fine particles at high temperatures.

Oxide particles in ODS steels may serve as strong absorption sinks for point defects and nucleation sites for He bubbles in irradiation environments, reducing the accumulation of irradiation defects [7]. However, in recent reports, there are varying conclusions about the irradiation stability of oxide particles. For example, a decrease in the size of oxide particles in ODS materials with increasing irradiation dose has been reported, although it is still claimed that the oxide particles remain stable under irradiation [8, 9]. Zhang et al. [10] performed dual-beam irradiation of austenitic ODS steel and conclude that tiny oxide particles are unstable at high doses. Further, Lescoat et al. [11] reported the coarsening of oxide particles with increasing irradiation dose, and the oxide particles undergo compositional changes after irradiation. Therefore, it is crucial to further research about the irradiation response of ODS nano-particles under different irradiation conditions in order to understand about the irradiation behaviors of ODS Au-SSs. In addition, the irradiation hardening effect of ODS steels is more complicated than conventional steels, and multiple aspects including the effect of the type of dislocation loops have to be considered in a successful modeling of irradiation hardening effect of ODS steels [12–14].

In this study, D/He ion irradiation were performed on 15-15Ti and ODS samples to compare the irradiation response before and after irradiation, taking into account of different types of loops. When evaluating the microstructural irradia-

* Supported by the National Natural Science Foundation of China (12105017)

† Corresponding author, xuchi@bnu.edu.cn

‡ Corresponding author, zhenfeng_tong@ncepu.edu.cn

tion response of 15-15Ti ODS samples under irradiation, the following points are focused on: (1) stability of oxide particles after irradiation, and changes in particle size, density, shape and composition before and after irradiation; (2) the role of oxide particles in the irradiation of materials and the mechanism of interaction with irradiation defects; (3) radiation induced segregation (RIS) of oxide particles with the matrix and at grain boundaries; (4) irradiation hardening and obstacle parameters of different irradiation defects.

## 2. Experimental procedures

The 15-15Ti and 15-15Ti ODS steel with chemical compositions (wt.%) of Fe-15Cr-15Ni-2Mo-0.2Ti and Fe-15Cr-15Ni-2Mo-0.2Ti-0.4Zr-0.35$Y_2O_3$, respectively, are studied in this research. The 15-15Ti material was prepared by argon atomization method with further refined grains. The ODS material was prepared by mechanically alloying the mixture of 15-15Ti, Zr and $Y_2O_3$ powders through high-energy ball milling and sintering. Transmission electron microscopy (TEM) samples with a diameter of 3 mm and a thickness of about 70 $\mu$m were prepared through mechanical cutting, grinding, polishing and stamping, and then were perforated by twin-jet electropolishing using a mixed solution (10 vol. % perchloric acid methanol solution) at conditions of -50 $\sim$ -40 °C, 30 V voltage.

TEM characterization was performed using a FEI Tecnai TF20 field-emission transmission electron microscope operated at 200 kV. TEM characterization techniques include bright field imaging (BF), weak beam dark field imaging (WBDF), and selected area electron diffraction (SAED) to characterize the microstructure of the material. The rel-rod dark field (RRDF) imaging technique [15] was applied to quantitatively characterize the observed Frank dislocation loops (FDLs), the dark field images were taken by the center darkfield, which used the diffraction streak near the [011] zone axis between the {200} and {111} diffraction spots. Morphological and compositional analysis of precipitates contained in the samples using scanning transmission electron microscopy high angle annular dark field (STEM-HAADF) coupled with energy dispersive X-ray spectroscopy (EDXS), and compositional distribution analysis near grain boundaries. The sample was tilted 15 degrees along the $\alpha$-axis during spectroscopic analysis. In order to reveal voids and bubbles, phase contrast (Fresnel Fringes) is introduced by adjusting the focus under the BF image. Limited by the TEM resolution, voids and bubbles that are too small (<1 nm) cannot be observed.

The ion irradiation experiments are performed on a BNU-400 high-throughput ion implanter at Beijing Normal University (Beijing, China). The vacuum was maintained at $5\times10^{-4}$ Pa during the irradiation process. A schematic diagram of the ion irradiation sample stage is shown in Fig. 1, in which the main thermocouple and the cooling system can control the temperature, and the K thermocouple is used for precise measurement of the sample temperature. Using SRIM 2013 software, the radiation damage and the depth distribution of the ions were calculated using the Ion Distribution and Quick Calculation of Damage model based on the Kinchin-Peace model, with the displacement threshold energy as recommended in the literature [16], and plotted in Fig. 2. The detailed irradiation conditions are listed in Table 1. The thickness of the observable region of the sample is about 100 nm, and the dose is calculated as the average dose, similarly, the concentration of He is about 13400 appm.

Table 1. Irradiation condition and average dose.

| Ion Energy (keV) | Temperature (°C) | Flux (ions/cm$^2$) | Average Dose (dpa) |
|---|---|---|---|
| $D^+$(100) | R.T. | $1\times10^{17}$ | $\sim$0.65 |
| $He^+$(50) | R.T. | $0.75\times10^{17}$ | $\sim$1.14 |

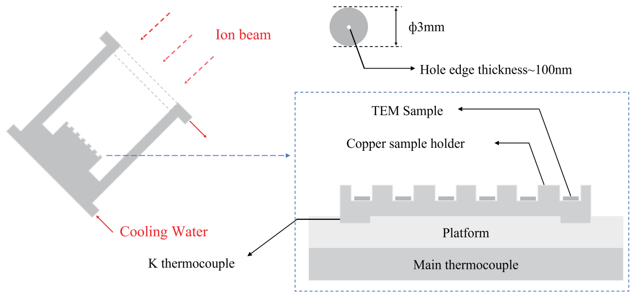


Fig. 1. Schematic diagram of the ion irradiation sample stage.

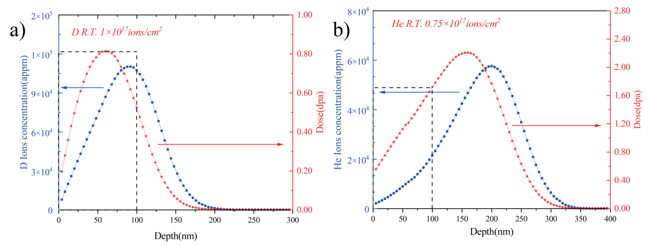


Fig. 2. Irradiation dose and distribution of ions with depth in (a) $D^+$, (b) $He^+$ irradiated samples simulated by SRIM 2013 software.

## 3. Results

### 3.1. Stability of oxide particles under different irradiation conditions

Pre-irradiation characterizations of the ODS samples reveal that there are two types of oxide particles in the samples, which are the $Al_2O_3$ particles and Y-Zr-O particles. The mean sizes and densities of the oxide particles in the pristine and irradiated ODS samples were counted and as shown in Table. 2. At low irradiation doses, as shown in Fig. 3(a-c), the diameters and densities of the oxide particles are almost unchanged, basically maintains a diameter of 10 nm and a

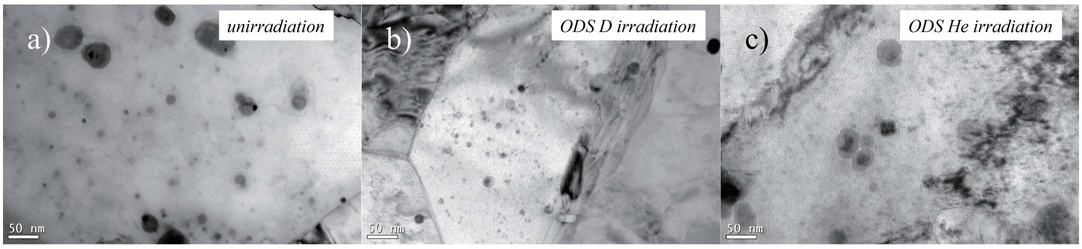


Fig. 3. Bright field images of oxide particles a) unirradiation; b) D irradiation; c) He irradiation.

Table 2. The diameter and density of oxide particles in ODS sample under different irradiation conditions.

| Irradiation condition | Oxide particle mean size(nm) | Oxide particle density(/m$^3$) |
|---|---|---|
| unirradiated | 9.97±0.04 | 4.49±0.45Œ$\times 10^{22}$ |
| ∼0.65dpa | 10.20±0.67 | 4±0.4Œ$\times 10^{22}$ |
| ∼1.14dpa | 10.14±0.52 | 4.02±0.4Œ$\times 10^{22}$ |

density of $4\times10^{22}$/m$^3$ (the smaller oxide particles appear to be blurred due to the presence of high densities He bubbles and dislocation loops in Fig. 3c). The compositions and morphologies of the oxide particles also do not change significantly according to the composition analysis.

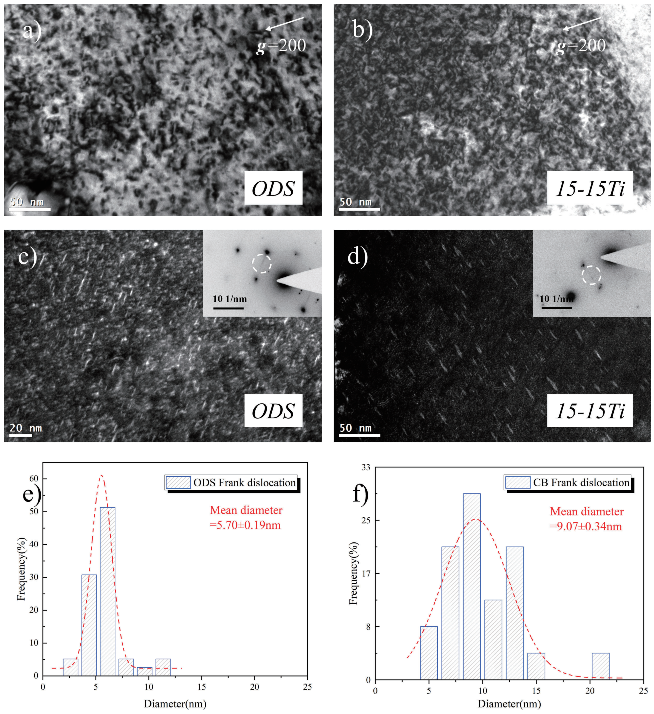


Fig. 4. (a, b) Bright field images of dislocation loops after He$^+$ irradiation to 1.14 dpa for (a) ODS sample and b) 15-15Ti sample. (c-f) RRDF images of FDLs and histograms of loop diameters for (c, e) ODS sample; (d, f) 15-15Ti sample.

### 3.2. Characterizations of dislocation loops after irradiation

In face-centered cubic (FCC) crystals, two types of dislocation loops can be generated after irradiation, which are the perfect dislocation loops (PDLs) with a Burgers vector of **a**/2[011] and the faulted Frank dislocation loops (FDLs) with a Burgers vector of **a**/3<111>. The dislocation loops in the sample after He ion irradiation were characterized under the ***g/3g***, ***g***200 weak-beam condition near the [011] axis, as shown in Fig. 4(a, b). After irradiation, dislocation loops with a diameter of about 5 nm can be observed in both samples. Besides, defect clusters such as the "black-dot" defects can also be observed in Fig. 4(a, b). FDLs are observed under the RRDF technique as shown in Fig. 4(c, d). The total number of FDLs is obtained by multiplying a factor of 4 over the counted loops number, assuming an internal isotropy of the material. The diameters and densities of dislocation loops were counted after He ion irradiation, considering the loops size error, using the standard error of the mean, and the uncentainty of the loops densities was estimated to be ±10% of the measured values, taking into account the uncertainty in the loops diameter counts and the thickness measurements. Statistically, the densities and diameters of **a**/3<111> loops are $1.65\times10^{22}$/m$^3$ and 5.7 nm in ODS sample and $1.25\times10^{22}$/m$^3$ and 9.07 nm in 15-15Ti sample, respectively. Whereas there is a significant difference in the total densities and diameters, are $1.89\times10^{22}$/m$^3$ and 5.71 nm in ODS sample and $4.75\times10^{22}$/m$^3$ and 5.84 nm in 15-15Ti sample, dislocation loop density in the post-irradiation ODS samples was comprehensively less than that of the 15-15 TI samples, the specific data is listed in Table. 3 and Fig. 5.

The dislocation loops in the sample after D ion irradiation were characterized using the WBDF technique under the ***g/3g***, ***g***=200/±[$\bar{1}\bar{1}$1] near the [011] axis, as shown in Fig. 6. Clusters of defects that resemble "black-dot" are observed. Under these characterization conditions, the "black-dot" defects are visible in all three ***g*** vectors and can be recognized as FDLs (***b***=**a**/3<111>). The bright field (BF) image after irradiation shows that the distribution of dislocation loops in 15-15Ti sample is uniform in general, except that there are differences in the size of the "black-dot" in different areas

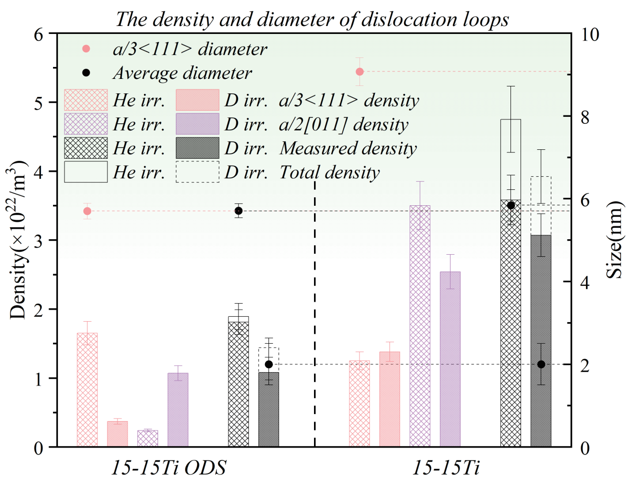


Fig. 5. The histogram image of the density and diamater of dislocation loops.

(possibly slight differences in thickness), while their distributions in the ODS sample are random. Also, in order to avoid the effect of precipitates and oxide particles on the dislocation loops affecting the statistics of the dislocation loops density, the BF images of only the matrix at the same diffraction ***g*** vector were selected for comparison. Where oxide particles are present, the distribution of "black-dot" clusters is more uneven, with many directly around or on particles, as can be seen in Fig. 6a, where the black arrows indicate particles and the red arrows refer to "black-dot" clusters.

As shown in Fig. 6(a-f), the dislocation loops are small and all present the "black-dot" contrasts in the two types of samples after the irradiation. The loop sizes are difficult to estimate precisely and are approximated to be $\sim 2\pm0.5$ nm in diameter. The loops densities were counted and treated as the same way with the He ion irradiation. The densities of **a**/3<111> loops are $0.37\times10^{22}/\text{m}^3$ in ODS sample and $1.38\times10^{22}/\text{m}^3$ in 15-15Ti sample, respectively. Whereas the total densities and diameters are $1.44\times10^{22}/\text{m}^3$ and 2 nm in ODS sample and $3.92\times10^{22}/\text{m}^3$ and 2 nm in 15-15Ti sample, the specific statistics are listed in Table. 3 and Fig. 5. The histogram of the density of dislocation loops irradiated to 0.65dpa and the density of FDLs is plotted in Fig. 6h, and significant difference in the density can be seen, with the ODS sample has a lower density of dislocation loops than 15-15Ti sample.

### 3.3. Characterizations of He bubbles

The BF image of He bubble in the sample irradiated by He ions can be seen in Fig. 7. The He bubble distribution in the ODS samples is not completely uniform, with higher He bubble densities around the oxide particles and lower He bubble densities in the neighborhood of the oxide particles and in the matrix, whereas the distribution of He bubbles in the 15-15Ti samples is generally uniform. The diameter and density of He bubbles were counted as 1.83 nm and $1.56\times10^{23}/\text{m}^3$ in the ODS sample and 1.41 nm and $8.13\times10^{23}/\text{m}^3$ in the 15-15Ti sample, the specific statistics are listed in Table. 4. The diameters under the standard error of taking the mean are almost the same, while the He bubble density of the 15-15Ti sample is much higher than that of the ODS sample.

Fig. 8(a-d) shows the BF images of He bubble distribution at the oxide particles and precipitates and grain boundary as absorption sinks. Small-sized He bubble (<2 nm) are observed to nucleate around the sink trap, as seen in the lighter contrast regions around the oxide particle in Fig. 8a, indicated by the white arrows in Fig. 8(b, c) and at the grain boundary in the middle of the two white dashed lines (Fig. 8d). Especially, the phenomenon of one He bubble after another is visible at grain boundary in the absence or near absence of oxide particles.

### 3.4. Radiation induced segregation

In the present study, segregation of elemental compositions was observed at grain boundaries after both He and D ion irradiation and plotted in Fig. 9(a-d). Due to the average concentration of elements is not exactly the same everywhere in the material, the degree of segregation be tantamount to difference in elemental concentration max/average elemental concentration is defined as a measure of the degree of segregation of the elements near the grain boundaries, and the error in the degree of segregation is estimated to be $\pm10\%$ of the measured value and plotted in Fig. 9e.

After the above treatment, it can be clearly seen that the ODS material has a lower degree of irradiation segregation than the 15-15Ti sample, the atomic ratios of Cr and Ni elements in the ODS sample varied by $5\sim10$ % than in the 15-15Ti sample. Besides, the regions where the elements have varied are roughly all about 10 nm, and both show the common phenomenon of irradiation segregation of austenitic stainless steel, that is, Ni enriched and Cr depletion under all irradiation conditions. More noteworthy is the ODS sample under He irradiation, there are two smaller peaks next to the main segregation peak.

### 3.5. Radiation induced segregation

The results of the microhardness of the materials obtained by nanoindentation experiments. Due to the presence of indentation size effect (ISE), the hardness value of the near-surface of the material cannot be accurately obtained. For accurately obtaining the hardness values, using a homogeneous material hardness model based on geometrically necessary dislocations, i.e., the Nix-Gao model, with the expression shown in Eq. 1 [17]:

$$H = H_0\sqrt{1+\frac{h^*}{h}} \tag{1}$$

Table 3. The density and diameter of dislocation loops.

| Irradiation conditions | Materials | **a**/3<111> Density ($\times 10^{22}$/m$^3$) | **a**/3<111> Diameter (nm) | **a**/2[011] Density ($\times 10^{22}$/m$^3$) | Measured Density ($\times 10^{22}$/m$^3$) | Total Density ($\times 10^{22}$/m$^3$) | Diameter (nm) |
|---|---|---|---|---|---|---|---|
| $He^+$ | ODS | 1.65±0.17 | 5.70±0.19 | 0.24±0.22 | 1.81±0.18 | 1.89±0.19 | 5.71±0.17 |
| 1.14dpa | 15-15Ti | 1.25±0.13 | 9.07±0.34 | 3.50±0.35 | 3.58±0.36 | 4.75±0.48 | 5.84±0.38 |
| $D^+$ | ODS | 0.37±0.04 | N/A | 1.07±0.11 | 1.08±0.11 | 1.44±0.14 | 2±0.5 |
| 0.65dpa | 15-15Ti | 1.38±0.14 | N/A | 2.54±0.25 | 3.07±0.31 | 3.92±0.39 | 2±0.5 |

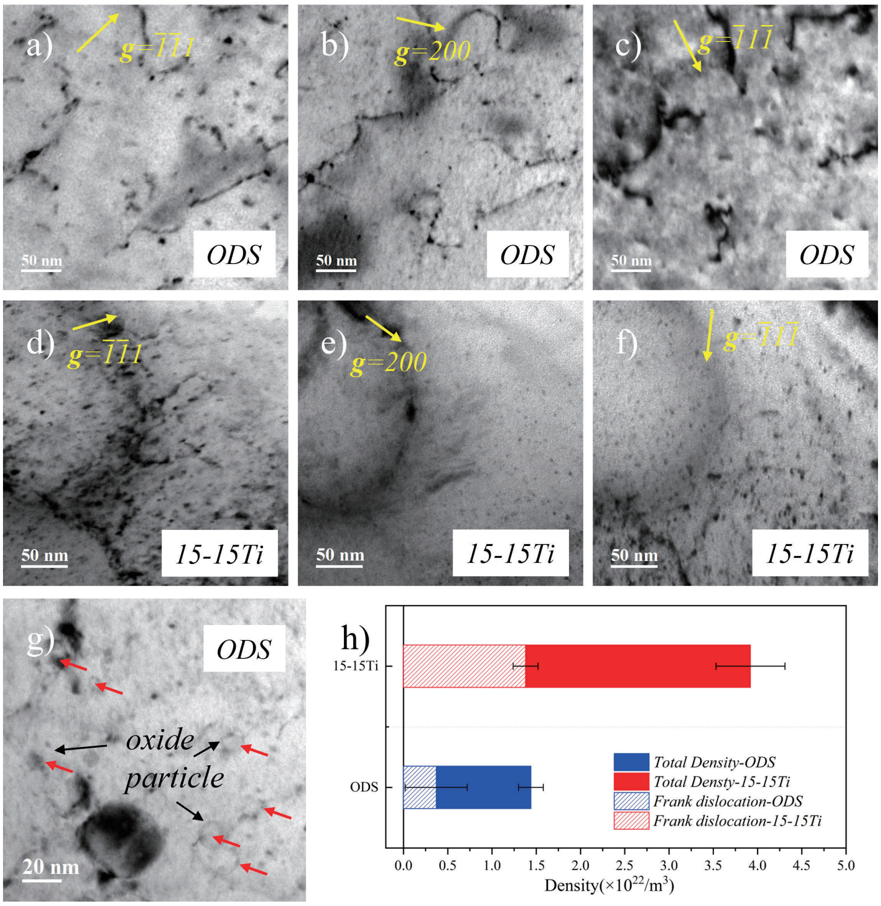


Fig. 6. Bright field images of dislocation loops in different samples after $D^+$ irradiation to 0.65 dpa, a), b), c) ODS sample; d), e), f) 15-15Ti sample. g) BF characterization of the nucleation of dislocation loops on oxide particles. h) Histogram of total and Frank-type dislocation loop densities in the two types of samples.

Table 4. The He bubble mean diameter and density in ODS sample and 15-15Ti samples.

| Sample | He bubble mean diameter (nm) | He bubble Density ($\times 10^{23}$/m$^3$) |
|---|---|---|
| ODS | 1.83±0.35 | 1.56±0.11 |
| 15-15Ti | 1.41±0.05 | 8.13±0.81 |

Table 5. Hardness of 15-15Ti and ODS samples before and after irradiation.

| Sample | Unirradiated (GPa) | D irradiation (GPa) | He irradiation (GPa) |
|---|---|---|---|
| 15-15Ti | 4.8 | 5.05 | 5.81 |
| $\Delta H$ | - | 0.25 | 1.01 |
| ODS | 5.15 | 5.39 | 5.74 |
| $\Delta H$ | - | 0.24 | 0.59 |

Where $h$ is the depth of the indentation, $H_0$ is the hardness value at infinite depth of the indentation, i.e., the true hardness value of the material, and $h^*$ is a constant related only to the properties of the material itself and the shape of the indenter. The hardness values for the irradiation layer can be obtained by plotting with $H^2$ as the vertical coordinate

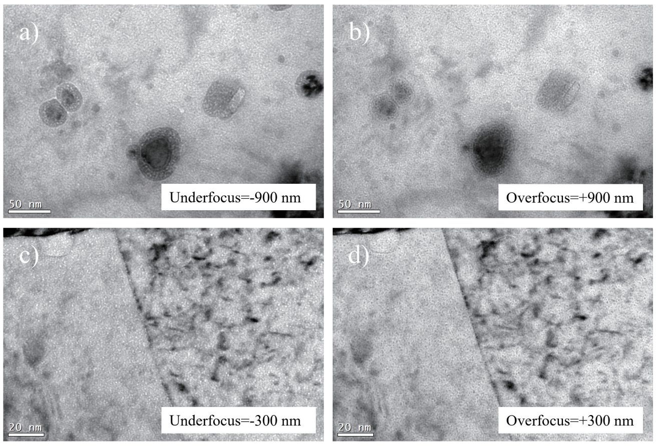


Fig. 7. He bubble bright field image a), b) ODS sample; c), d) 15-15Ti sample.

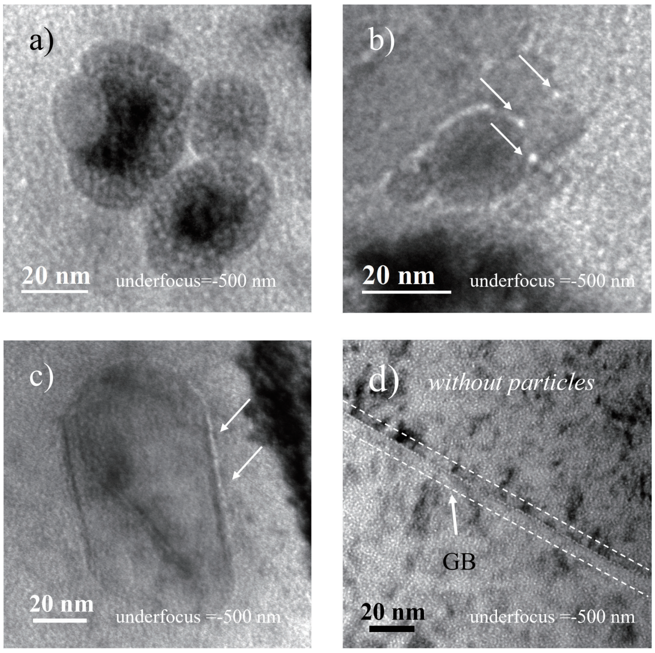


Fig. 8. Helium bubble trapped by a), b) oxide particle; c) precipitate; d) grain boundary.

and *1/h* as the abscissa coordinate, as shown in Fig. 10(a, b). The hardness values of 15-15Ti and ODS sample are 4.8 GPa and 5.15 GPa when unirradiated, after D irradiation, are 5.05 GPa and 5.39 GPa, the hardness increases are 0.25 GPa and 1.01 GPa, respectively, and after He irradiation, are 5.81 GPa and 5.74 GPa, the hardness increases are 0.24 GPa and 0.59 GPa, respectively. The specific dates are listed in Table. 5 and Fig. 10c.

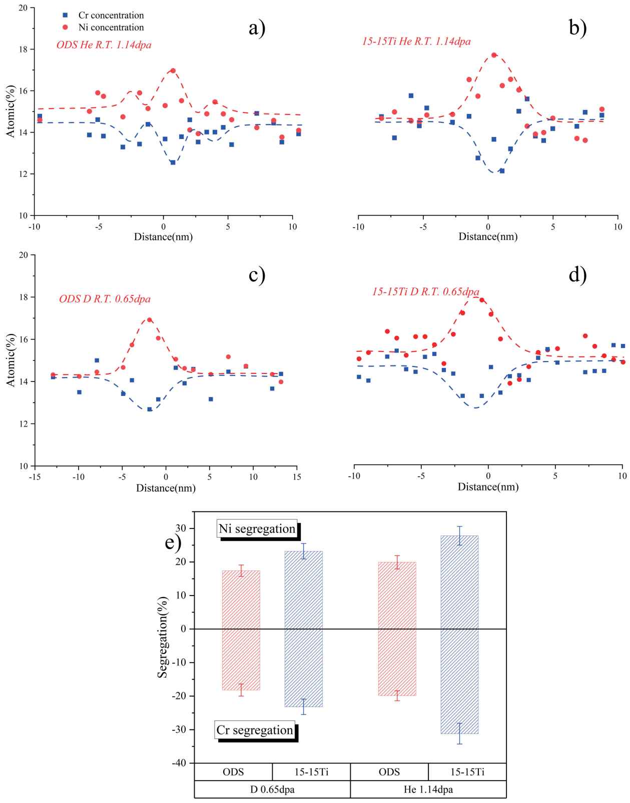


Fig. 9. RIS in two materials under different irradiation conditions.

## 4. Discussion

### 4.1. Dislocation evolution and irradiation hardening

In the irradiated austenitic stainless steels, the crystal defects are mainly composed of the Frank dislocation loops (FDLs), which are stacking fault dislocation loops. Depending on the stacking faults energy (SFE) of the material, prismatic dislocation loops (PDLs) can also be generated through irradiations. In addition, PDLs with low energy can be generated by the unfaulting reaction of FDLs [18]. PDLs are glissle and can slip and climb, whereas FDLs are sessile loops that can only move through dislocation climbing. The slip of dislocations in the material reduces the yield strength of the material. In principle, the FDLs that are not easily slipped could act as obstacle to PDLs. From this perspective, it can be inferred that the presence of FDLs after irradiation may assist in mitigating thermal creep in Fast breeder reactors [19], and with the irradiation process, FDLs grow predominantly by absorbing point defects but not in the same manner as PDLs, resulting in a lower density but larger size and a more random distribution than PDLs, as seen in this and other study [20]. On the basis of $\boldsymbol{g} \cdot \boldsymbol{b}$=0, FDLs (**a**/3<111>) are visible under all $\boldsymbol{g}$ vector in the [011] zone axis. Through tilting the $\boldsymbol{g}$ vector, no significant variation in occupancy ratio, the density of FDLs in the 15-15Ti sample is considered to remain unchanged (Fig. 5d-f). In contrast, the percentage of FDLs in

the ODS sample varied with the ***g*** (Fig. 5a-c). As a result, the irradiation defects such as "black-dot" cannot simply be recognized as FDLs, and that only "black-dot" are more likely to be FDLs.

He ion irradiation introduces helium atoms into the material, leading to the formation of He-vacancy clusters that capture self-interstitial atoms (SIAs) and accelerate the nucleation of dislocation loops, which is a non-negligible influence on the increase in the density of dislocation loops by He ion irradiation [21]. The information on dislocation loops after irradiation is summarized in Table. 3 and Fig. 6h. Obviously, the dislocation density in both samples increases with the increase of the irradiation dose, with a significantly lower dislocation density in the ODS sample than the 15-15Ti sample. Fig. 6g illustrates the nucleation of dislocation loops on the oxide particles, indicating that the oxide particle/matrix interface serves as an absorption sink of irradiation defects, similar as that reported in previous studies [22, 23]. The study by Liu et al [24] indicates that oxide particles efficiently absorb freely migrating defects and inhibit radiation enhanced diffusion, thereby reducing the density of dislocation loops by limiting the movement of defect clusters. This suggests that the presence of oxide particles in the ODS sample is one of the key factors contributing to its lower dislocation density compared to the 15-15Ti sample.

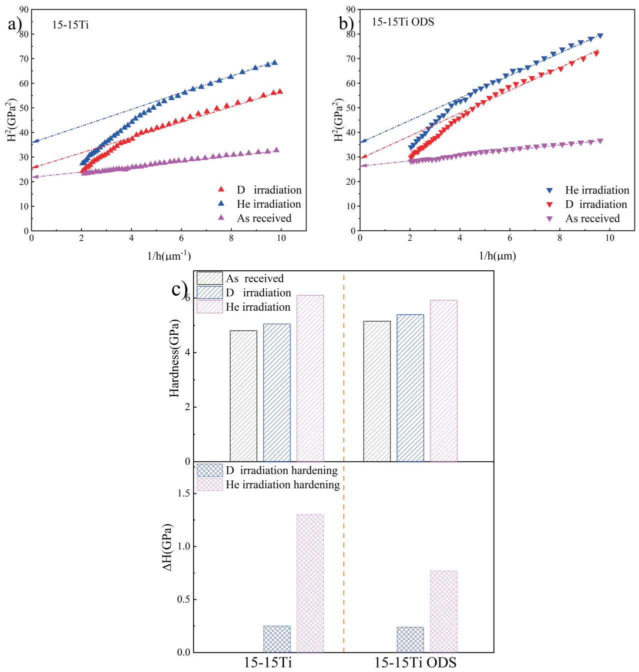


Fig. 10. (a, b)$H^2$-$1/h$ plot of 15-15Ti and ODS samples; (c) histogram of hardness and hardened value added.

Irradiation hardening is observed in all irradiated samples as shown in Table. 5. There are numerous models to predict the change in dislocation glide resistance induced by irradiation defects. After a comparison, a dispersed barrier hardening (DBH) model based on Orowan's theory [25] and Friedel model [26] are applied to predict the hardening due to dislocation loops and bubbles, respectively. The hardening values of the two materials are nearly identical under D ion irradiation, despite significant differences in dislocation loop densities, indicating that hardening is not solely caused by dislocation loops. Gas bubbles are also observed in the ODS sample (Fig. 11), while none are detected in the 15-15Ti sample. The density and size of the bubbles in the ODS matrix are approximately $2.17\times10^{22}$/m$^3$ and 3 nm, respectively.

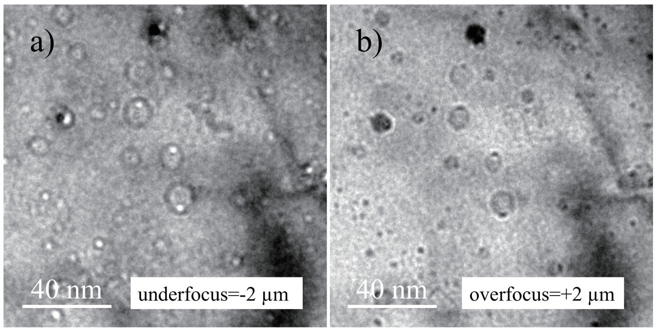


Fig. 11. Irradiation induced gas bubbles in ODS sample after D$^+$ irradiation characterized in different focus state: (a) underfocus ($\Delta f$ = -2 $\mu$m); (b) overfocus ($\Delta f$ = 2 $\mu$m).

Assuming the shape of the He bubbles is spherical and using the measured average bubble radius *r*. The characteristics of the He bubbles needed for the model are measured based on TEM analysis and these are summarized in Table. 4, as given $N_{bubble}$, we determine the center-to-center bubble spacing via: $l$=1/(2$rN_{bubble}$)$^{1/2}$. According to Friedel model, the critical $\Delta\tau$ for a dislocation to bypass a He bubble in its glide plane is [26]:

$$\Delta\tau = \frac{Gb}{2\pi l_s} \ln \frac{l_s}{r\sqrt{\cos\varphi_c}} (\cos\varphi_c)^{3/2} \tag{2}$$

Among these, where $l_s$=$l$-$2r$ is the bubble surface spacing, $G$ is the shear modulus $G$=82 GPa [27], and $b$ is the value of the Burgers vector ($b$=0.248 nm). The angle $\varphi_c$ is half critical bow-out angle of the dislocation cutting an obstacle and is given by $\cos\varphi_c = ln(\alpha\bar{D}/b)/ln(l_s/b)$, where $1/\bar{D} = 1/D_b + 1/l_s$, $D_b$=$2r$ is the diameter of He bubbles and $\bar{D}$ is a harmonic mean of $l_s$ and $D_b$ [26]. In particular, D gas bubble is treated like He bubble. Applying the model for two materials, giving $\varphi_c$=59.1° for ODS (D gas bubble), $\varphi_c$=58.9° for ODS (He bubble) and 57.8° for 15-15Ti (He bubble), and the corresponding $\Delta\tau$ is 0.04GPa, 0.11 GPa and 0.20 GPa.

Meanwhile, according to the dispersed barrier hardening (DBH) model based on Orowan's theory:

$$\Delta H = \alpha M \mu b \sqrt{Nd} \tag{3}$$

Among these, the Taylor factor $M$=3.06, $\mu$ is the shear modulus, $\alpha$ is the obstacle strength parameter, $N$ and $d$ are the diameter and density of the obstacles, respectively. Based on the value of hardening due to the bubbles, accord-

ing to Eq. 3, the obstacle strength parameter $\alpha_{bubble}$~0.08, $\alpha_{He}$~0.10 (15-15Ti) and $\alpha_{He}$~0.13 (ODS) are got. The density and size of dislocation loops needed for Eq. 3 are presented in Table. 3. Considering that bubbles also contribute partially to hardening, as well as having discussed previously that different types of dislocation loops hold different energies and may contribute differently to hardening. In Lin's work [28], the obstacle parameters and factors influencing different dislocation loop types are investigated in terms of atomic dimensions. As a conclusion, different dislocation loop types do have different obstacle parameters. In addition to this, the interaction of different types of dislocation loops affects irradiation hardening [29]. On the other hand, inconsistency in the obstacle parameters of He bubble in different materials has been mentioned earlier in several works [30–33]. In this case, Eq. 4 ~ Eq. 6 can be obtained from Eq. 3:

$$\begin{aligned} \Delta H &= \Delta H_{dislocation} + \Delta H_{bubble} \\ &= \alpha_{black-dot} M \mu b \sqrt{Nd} + \Delta\tau_{bubble} \end{aligned} \tag{4}$$

$$\begin{aligned} \Delta H_{15-15Ti}(He) &= \Delta H_{dislocation} + \Delta H_{He\,bubble} \\ &= \alpha_{a/3<111>} M \mu b \sqrt{N_{a/3<111>} d_{a/3<111>}} \\ &+ \alpha_{a/2[011]} M \mu b \sqrt{N_{a/2[011]} d_{a/2[011]}} + \Delta\tau_{He\,bubble} \end{aligned} \tag{5}$$

$$\begin{aligned} \Delta H_{15-15TiODS}(He) &= \Delta H_{dislocation} + \Delta H_{He\,bubble} \\ &= \alpha_{a/3<111>} M \mu b \sqrt{N_{a/3<111>} d_{a/3<111>}} \\ &+ \alpha_{a/2[011]} M \mu b \sqrt{N_{a/2[011]} d_{a/2[011]}} + \Delta\tau_{He\,bubble} \end{aligned} \tag{6}$$

The obstacle strength parameter $\alpha_{black-dot}$ of ~ 0.45 in 15-15Ti sample is calculated, where $\alpha_{black-dot}$ in ODS sample, $\alpha_{a/3<111>}$~0.63, $\alpha_{a/2[011]}$~0.45 according to Eq. 4 ~ Eq. 6. Although various previous studies have demonstrated that dislocation loops are generally considered weak obstacle, despite their wide range of reported values (0.15-0.75) [34]. In addition to this, in complete considerations by the contributors to the hardening like oxygen-vacancy complexes [35], as well as experimental errors, may have biased the barrier factors calculated based on the results of this experiment.

The obstacle parameter for different defects within a material is an interval range, due to the different internal compositions of the material [36]. Consequently, rather than defining the obstacle strength parameter of the dislocation loops and bubbles with and exact value, a suitable range shall be used. Then, expanding the data to the range in conjunction with previous studies, in which $\alpha_{dislocation\ loop}$ (0.34-0.56) [31], to summarize, weak obstacle $\alpha_{bubble}$(0.08-0.13), medium to strong obstacle $\alpha_{dislocation\ loop}$(0.45-0.56).

### 4.2. He bubble

Generally, in ODS materials, grain boundaries, precipitates, nanoparticles, etc. are absorption sinks for He bubbles (see Fig. 8). After He is generated in the matrix, it will be captured by the oxide particles and precipitates and grain boundary at the interfaces with the matrix and thus nucleated at these places. The presence of precipitates and oxide particles reduces the nucleation of He bubbles at grain boundaries, thus reducing the possibility of He embrittlement [7]. The TEM characterization in the current experiment revealed a low number of precipitates in the ODS sample, as a result, only grain boundaries and oxide particles are considered. The grain sizes of the two samples are measured as approximately 504 nm for ODS and 1 $\mu$m for 15-15Ti. Details regarding the oxide particles are provided in Table. 2. The sink strength for grain boundary and oxide particle/matrix interface can be simply calculated using Eq. 7 and 8 [37, 38]:

$$S_o = 4\pi N[0.3(4\pi r^2)^{0.5}] \tag{7}$$

$$S_g = 15/h^2 \tag{8}$$

Where $N$ is the oxide particle number density, $r$ is the average diameter of oxide particles, $h$ is the average grain size. The sink strength results are $S_o$~$6.77\times10^{14}$/m$^2$, $S_g$~$5.9\times10^{13}$/m$^2$ (ODS) and $1.5\times10^{13}$/m$^2$ (15-15Ti), while the sink strength of the oxide particles is significantly higher than that of the grain boundaries. In this experiment no He bubble depletion region is observed as mentioned by Tong et al [39], neither is nucleation and growth of He bubbles at grain boundaries observed as mentioned by Zhang et al [10]. Based on this, we can infer that the oxide particles serve as the primary sinks for He bubbles under the irradiation conditions studied in this paper. They are the main contributors to the lower helium bubble density observed in the ODS samples compared to the 15-15Ti samples.

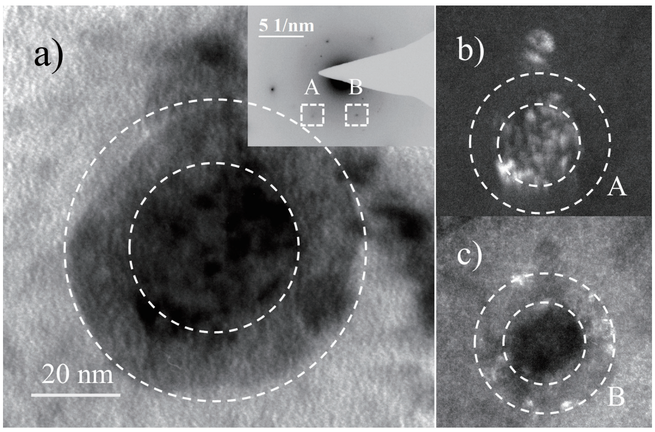


Fig. 12. a) enlarged an oxide particle, central dark field analysis of ODS particles b) centered on the A diffraction spot; c) centered on the B diffraction spot.

Meanwhile, a number of different morphologies of particles adsorbing He bubbles are found to exist within the matrix, as seen in Fig. 8(a, b). Obviously, there are tiny He bubbles in the lighter contrast regions around the particle, and slightly larger individual He bubble on the particle. Oxide particles were subjected to SAED, and the diffracted spots were then selected and moved to the center of the beam to form a central dark field to analyze different regions of orientation. In the center dark field image analysis (Fig. 12), it is found that the diffraction points corresponding to the central low density He bubbles region and the surrounding high He bubbles region are different. It is speculated that the different He bubbles adsorption densities are caused by the different orientations, or to describe different lattice distances [40].

### 4.3. Radiation induced segregation

Since different ions were used in the irradiation experiment, it is important to consider their potential impacts on elemental segregations. Lin et al [41] demonstrated that the implanted helium atoms have no significant effect on the segregation of Cr and Ni elements when predicting radiation-induced segregation (RIS) behavior in alloys using the vacancy mechanism and the interstitial binding mechanism. It can be inferred that the RIS in this study is independent of the incident particles. As shown in Fig. 9, the 15-15Ti and ODS samples align well with the results reported for other austenitic stainless steels, exhibiting Ni enrichment and Cr depletion, interpreted as an inverse Kirkendall effect [15, 42]. In the segregation results, a phenomenon similar to "satellite peaks" was observed only in the ODS sample under He irradiation, which may be due to the difference in the type of grain boundaries [43, 44]. Additionally, the degree of segregation increases with the increase of irradiation dose, despite of the fact that the increase of segregation in ODS material is significantly lower than that of 15-15Ti samples. However, RIS does not monotonically increase with increasing irradiation dose, and there will be a saturation value [45] or the formation of precipitates at grain boundaries [10] at high irradiation doses.

The sink strength of oxide particles and grain boundaries was discussed in the previous section. To assess their contribution to counteracting RIS in ODS samples, an approximation of $r_o/r_g \approx S_o/S_g \approx 10$ was used, where $r_o$ is the sink radius of the oxide particles and $r_g$ is the sink radius of the grain boundaries. From Fig. 9(a-d), it can be approximated that $r_g \approx 5$ nm, while $r_o \approx 50$ nm. The distribution of oxide particles was analyzed, revealing that around 5-10% of the particles are located near grain boundaries (within 50 nm of the boundaries). In conventional polycrystalline materials, grain boundaries are the primary sinks for vacancies, leading to element depletion or enrichment at these boundaries for those that diffuse via forming atom-vacancy complexes [46]. However, in ODS steels, the interface of particle/matrix also acts as a significant vacancy sink, particularly for the 5-10% of oxide particles located near the grain boundaries, which possess high sink strength $\sim 6.77\times10^{13}/m^2$ than GBs $\sim 5.9\times10^{13}/m^2$ and can influence the RIS at GBs. Thus, it is believed that oxide particles contribute to mitigation of RIS to certain extents. Nevertheless, no obvious segregation of oxide particles was found in the experiments. Only a few oxide particles with altered compositions were found, which are not representative. In addition, one of the features of ODS materials prepared through mechanical alloying (MA) is the reduced grain size. It remains unclear whether the fine oxide particles or the reduced grain sizes play a dominant role in resisting RIS in the ODS materials.

## 5. Conclusion

Ion irradiation was carried out on 15-15Ti and 15-15Ti ODS samples, and irradiation defects such as dislocation loops and He bubbles, as well as radiation induced segregation and irradiation hardening were characterized. The following conclusions can be obtained:

1. Under the irradiation conditions studied in this paper, the ODS sample has a lower loop density compared to the 15-15Ti sample, mainly due to the contribution of oxide particles as absorption sinks.
2. Irradiation hardening occurred in all samples. The contribution to irradiation hardening mainly comes from two parts, including dislocation loops and bubbles introduced by ion irradiation. Bubbles are weak obstacle, and dislocation loops are medium to strong obstacle.
3. The distribution of He bubbles in the ODS samples after He ion irradiation is not completely uniform, with higher He bubble densities observed around the oxide particles and lower He bubble densities in the vicinity of the oxide particles and in the matrix, whereas the distribution of He bubbles in the 15-15Ti samples is generally uniform. The ODS samples exhibit a lower overall He bubble density, primarily due to the oxide particle/matrix interface acting as a sink, effectively trapping and reducing the formation of He bubble.
4. RIS occurs in all samples after irradiation. However, the ODS sample exhibits a lower degree of RIS compared to 15-15Ti sample, which is attributed to dual factors including the finer grains of ODS samples and the oxide particles/matrix interfaces that serve as defect sinks.

### Declaration of Competing Interest

The authors declare that they have no known competing financial interests or personal relationships that could have appeared to influence the work reported in this paper.

[1] A.V. Vatulin, A.V. Tselishchev, Structural steels for cores of fast neutron reactors. Met. Sci. Heat Treat. **46**, 463-468(2004). doi: 10.1007/s11041-005-0003-9

[2] S.J. Zinkle, J.T. Busby, Structural materials for fission & fusion energy. Mater. Today. **12**, 1219(2009). doi: 10.1016/S1369-7021(09)70294-9

[3] F.A. Garner, M.B. Toloczko, B.H. Sencer, Comparison of swelling and irradiation creep behavior of fcc-austenitic and bcc-ferritic/martensitic alloys at high neutron exposure. J. Nucl. Mater. **276**, 123142(2000). doi: 10.1016/S0022-3115(99)00225-1

[4] J. Sun, H. Tang, C. Wang et al., Effects of Alloying Elements and Microstructure on Stainless Steel Corrosion: A Review. Steel Res. Int. **93**, 2100450(2022). doi: 10.1002/srin.202100450

[5] J.S. Cheon, C.B. Lee, B.O. Lee et al., Sodium fast reactor evaluation: Core materials. J. Nucl. Mater. **392**, 324330(2009). doi: 10.1016/j.jnucmat.2009.03.021

[6] S.J. Zinkle, L.L. Snead, esigning Radiation Resistance in Materials for Fusion Energy. Annu. Rev. Mater. Res. **44**, 241267(2014). doi: 10.1146/annurev-matsci-070813-113627

[7] G.R. Odette, M.J. Alinger, B.D. Wirth, Recent Developments in Irradiation-Resistant Steels. Annu. Rev. Mater. Res. **38**, 471503(2008). doi: 10.1146/annurev.matsci.38.060407.130315

[8] M.-L. Lescoat, J. Ribis, A. Gentils et al., In situ TEM study of the stability of nano-oxides in ODS steels under ion-irradiation. J. Nucl. Mater. **428**, 176182(2012). doi: 10.1016/j.jnucmat.2011.12.009

[9] S. Santra, S. Amirthapandian, S. Balaji et al., Ion irradiation stability of oxide nano-particles in ODS alloys: TEM studies. J. Nucl. Mater. **528**, 151861(2020). doi: 10.1016/j.jnucmat.2019.151861

[10] H.K. Zhang, Z. Yao, Z. Zhou et al., Radiation induced microstructures in ODS 316 austenitic steel under dual-beam ions. J. Nucl. Mater. **455**, 242247(2014). doi: 10.1016/j.jnucmat.2014.06.024

[11] M.-L. Lescoat, J. Ribis, Y. Chen et al., Radiation-induced Ostwald ripening in oxide dispersion strengthened ferritic steels irradiated at high ion dose. Acta Mater. **78**, 328-340(2014). doi: 10.1016/j.actamat.2014.06.060

[12] Y.P. Wei, P.P. Liu, Y.M. Zhu et al., Evaluation of irradiation hardening and microstructure evolution under the synergistic interaction of He and subsequent Fe ions irradiation in CLAM steel. J. Alloys Compd. **676**, 481488(2016). doi: 10.1016/j.jallcom.2016.03.167

[13] Z. Tong, Y. Dai, The microstructure and tensile properties of ferritic/martensitic steels T91, Eurofer-97 and F82H irradiated up to 20 dpa in STIP-III. J. Nucl. Mater. **398**, 4348(2010). doi: 10.1016/j.jnucmat.2009.10.008

[14] Z. Tong, Y. Dai, Tensile properties of the ferritic martensitic steel F82H after irradiation in a spallation target. J. Nucl. Mater. **385**, 258261(2009).doi:10.1016/j.jnucmat.2008.12.015

[15] C. Xu, W.-Y. Chen, X et al., Effects of neutron irradiation and post-irradiation annealing on the microstructure of HT-UPS stainless steel. J. Nucl. Mater. **507**, 188197(2018). doi: 10.1016/j.jnucmat.2018.04.043

[16] G.S. Was, *Fundamentals of radiation materials science: metals and alloys*, 2nd edn. (Springer, New York, 2017). doi: 10.1007/978-1-4939-3438-6

[17] W.D. Nix, H. Gao, Indentation size effects in crystalline materials: A law for strain gradient plasticity. J. Mech. Phys. Solids **46**,411425(1998). doi: 10.1016/S0022-5096(97)00086-0

[18] D. Hull, D.J. Bacon, *Introduction to Dislocations*, 5th edn. (Butterworth-Heinemann, Oxford, 2011).doi: 10.1016/B978-0-08-096672-4.00005-0

[19] N. Khiara, F. Onimus, J.-P. Crocombette et al., A molecular dynamics study of a cascade induced irradiation creep mechanism in pure copper. J. Nucl. Mater. **560**,153518(2022). doi: 10.1016/j.jnucmat.2022.153518

[20] P. Xiu, Y.N. Osetsky, L. Jiang et al., Dislocation loop evolution and radiation hardening in nickel-based concentrated solid solution alloys. J. Nucl. Mater. **538**, 152247(2020). doi: 10.1016/j.jnucmat.2020.152247

[21] K. Arakawa, R. Imamura, K. Ohota et al., Evolution of point defect clusters in pure iron under low-energy $He^+$ irradiation. J. Appl. Phys. **89**, 47524757(2001). doi: 10.1063/1.1357785

[22] H. Oka, M. Watanabe, H. Kinoshita et al., In situ observation of damage structure in ODS austenitic steel during electron irradiation. J. Nucl. Mater. **417**, 279282(2011). doi: 10.1016/j.jnucmat.2010.12.156

[23] E. Aydogan, O. El-Atwani, M. Li et al., In-situ observation of nano-oxide and defect evolution in 14YWT alloys. Mater. Charact. **170**, 110686(2020). doi: 10.1016/j.matchar.2020.110686

[24] X. Liu, Y. Miao, M. Li et al., Radiation resistance of oxide dispersion strengthened alloys: Perspectives from in situ observations and rate theory calculations. Scr. Mater. **148**, 33-36(2018). doi: 10.1016/j.scriptamat.2018.01.018

[25] B.N. Singh, A.J.E. Foreman, H. Trinkaus, Radiation hardening revisited: role of intracascade clustering. J. Nucl. Mater. **249**, 103115(1997). doi: 10.1016/S0022-3115(97)00231-6

[26] Q.M. Wei, N. Li, N. Mara et al., Suppression of irradiation hardening in nanoscale V/Ag multilayers. Acta Mater. **59**, 63316340(2011). doi: 10.1016/j.actamat.2011.06.043

[27] S.A. Kim, W.L. Johnson, Elastic constants and internal friction of martensitic steel, ferritic-pearlitic steel, and $\alpha$-iron. Mater. Sci. Eng. A, **452-453**, 633639(2007). doi: 10.1016/j.msea.2006.11.147

[28] P. Lin, J. Nie, Y. Lu et al., The effects of different factors on obstacle strength of irradiation defects: An atomistic study. Nucl. Eng. Technol. **56**, 22822291(2024). doi: 10.1016/j.net.2024.01.039

[29] M. Borde, L. Dupuy, A. Pivano et al., Interaction between 1/2<110>001 dislocations and 110 prismatic loops in uranium dioxide: Implications for strain-hardening under irradiation. Int. J. Plast. **168**, 103702(2023). doi: 10.1016/j.ijplas.2023.103702

[30] J.-T. Li, I.J. Beyerlein, W.-Z. Han, Helium irradiation-induced ultrahigh hardening in niobium. Acta Mater. **226**, 117656(2022). doi: 10.1016/j.actamat.2022.117656

[31] S. Zhang, S. Jiang, J. Lin et al., Study on irradiation hardening by He+ and subsequent V/self-ion irradiation in V-4Cr-4Ti under near-service conditions. Nucl. Mater. Energy **38**, 101624(2024). doi: 10.1016/j.nme.2024.101624

[32] C.-H. Su, C.-H. Zhang, Y.-T. Yang et al., Hardening of an ODS Ferritic Steel after Helium Implantation and Thermal Annealing*. Chin. Phys. Lett. **38**, 056102(2018). doi: 10.1088/0256-307X/35/5/056102

[33] H.H. Chen, Y.F. Zhao, J.Y. Zhang et al., He-ion irradiation effects on the microstructure stability and size-dependent mechanical behavior of high entropy alloy/Cu nanotwinned nanolaminates. Int. J. Plast. **133**, 102839(2020). doi: 10.1016/j.ijplas.2020.102839

[34] L. Tan, J.T. Busby, Formulating the strength factor $\alpha$ for improved predictability of radiation hardening. J. Nucl. Mater. **465**, 724730(2015). doi: 10.1016/j.jnucmat.2015.07.009

[35] C.L. Fu, M. Krmar, G.S. Painter et al., Vacancy Mechanism of High Oxygen Solubility and Nucleation of Stable Oxygen-

Enriched Clusters in Fe. Phys. Rev. Lett. **99**, 225502(2007). doi: 10.1103/PhysRevLett.99.225502
[36] F. Bergner, C. Pareige, M. Hernández-Mayoral et al., Application of a three-feature dispersed-barrier hardening model to neutron-irradiated FeCr model alloys. J. Nucl. Mater. **448**, 96102(2014). doi: 10.1016/j.jnucmat.2014.01.024
[37] K. y. Yu, C. Sun, Y. Chen et al., Superior tolerance of Ag/Ni multilayers against Kr ion irradiation: an in situ study. Philos. Mag. **93**, 35473562(2013). doi: 10.1080/14786435.2013.815378
[38] A.D. Brailsford, L.K. Mansur, The effect of precipitate-matrix interface sinks on the growth of voids in the matrix. J. Nucl. Mater. **104**, 14031408(1981). doi: 10.1016/0022-3115(82)90796-6
[39] Z. Tong, Y. Dai, W. Yang et al., Effects of radiation and He on microstructures of low active ferritic/martensitic steel F82H. Jinshu XuebaoActa Metall. Sin. **47**, 965970(2011). doi: 10.3724/SP.J.1037.2011.00208
[40] G. Y. Pan, Y. G. Li, Y. S. Zhang et al., First-principles investigation of the orientation influenced He dissolution and diffusion behaviors on W surfaces. RSC Adv. **7**, 2578925795(2017). doi: 10.1039/C7RA03281A
[41] W.T. Lin, G.M. Yeli, G. Wang et al., He-enhanced heterogeneity of radiation-induced segregation in FeNiCoCr high-entropy alloy. J. Mater. Sci. Technol. **101**, 226233(2022). doi: 10.1016/j.jmst.2021.05.053
[42] G.S. Was, J.P. Wharry, B. Frisbie et al., Assessment of radiation-induced segregation mechanisms in austenitic and ferriticmartensitic alloys. J. Nucl. Mater. **411**, 4150(2011). doi: 10.1016/j.jnucmat.2011.01.031
[43] C.M. Barr, G.A. Vetterick, K.A. Unocic et al., Anisotropic radiation-induced segregation in 316L austenitic stainless steel with grain boundary character. Acta Mater. **67**, 145155(2014). doi: 10.1016/j.actamat.2013.11.060
[44] J. Gao, F. Chen, X. Tang et al., Effects of grain boundary structures on primary radiation damage and radiation-induced segregation in austenitic stainless steel. J. Appl. Phys. **128**, 105304(2020). doi: 10.1063/5.0016404
[45] D.L. Damcott, T.R. Allen, G.S. Was, Dependence of radiation-induced segregation on dose, temperature and alloy composition in austenitic alloys. J. Nucl. Mater. **225**, 97107(1995). doi: 10.1016/0022-3115(94)00690-3
[46] W.Z. Han, M.J. Demkowicz, E.G. Fu et al., Effect of grain boundary character on sink efficiency. Acta Mater. **60**, 63416351(2012). doi: 10.1016/j.actamat.2012.08.009